Redox Biology 76 (2024) 103344

Contents lists available at ScienceDirect

Redox Biology

journal homepage: www.elsevier.com/locate/redox

CARM1 phosphorylation at S595 by p38γ MAPK drives ROS-mediated cellular senescence

Yena Cho [a,b], Yong Kee Kim [a,b,*]

[a] Muscle Physiome Research Center and Research Institute of Pharmaceutical Sciences, Sookmyung Women's University, Seoul, 04310, Republic of Korea
[b] College of Pharmacy, Sookmyung Women's University, Seoul, 04310, Republic of Korea

ARTICLE INFO

Keywords:
CARM1
p38γ MAPK
ROS
Mitochondrial homeostasis
Senescence

ABSTRACT

CARM1 is predominantly localized in the nucleus and plays a pivotal role in maintaining mitochondrial homeostasis by regulating gene expression. It suppresses mitochondrial biogenesis by downregulating *PGC-1α* and *TFAM* expression, while promoting mitochondrial fission through increased *DNM1L* expression. Under oxidative stress, CARM1 translocates to the cytoplasm, where it directly methylates DRP1 and accelerates mitochondrial fission, enhancing reactive oxygen species (ROS) production. Cytoplasmic localization of CARM1 is facilitated by its phosphorylation at S595 by ROS-activated p38γ MAPK, creating a positive feedback loop. Consequently, cytoplasmic CARM1 contributes to cellular senescence by altering mitochondrial dynamics and increasing ROS levels. This observation was supported by the increased cytoplasmic CARM1 levels and disrupted mitochondrial dynamics in the transformed 10T1/2 cells. Moreover, CARM1 inhibitors not only inhibit the proliferation of cancer cells but also induce apoptotic death in senescent cells. These findings highlight the potential of CARM1 inhibitors, particularly those targeting cytoplasmic functions, as novel strategies for eliminating cancer and senescent cells.

1. Introduction

Mitochondria are pivotal for cellular energy metabolism, apoptosis, and epigenetic modifications [1–4]. Maintenance of mitochondrial homeostasis involves tightly regulated biogenesis and dynamics [5,6]. Peroxisome proliferator–activated receptor gamma coactivator-1 alpha (PGC-1α) primarily governs mitochondrial biogenesis by upregulating the expression of nuclear respiratory factors 1/2 and subsequently enhancing mitochondrial transcription factor A (TFAM) expression [7,8]. TFAM plays a critical role in preserving mitochondrial DNA (mtDNA) integrity and copy number [8]. Mitochondrial dynamics, which are crucial for cellular function, involve fusion and fission events orchestrated by proteins, such as optic atrophy 1 and dynamin-related protein 1 (DRP1; encoded by *DNM1L*) [6]. Imbalances in fusion and fission disrupt the mitochondrial function and contribute to cellular senescence [9].

Arginine methylation, catalyzed by protein arginine methyltransferases (PRMTs) using *S*-adenosyl-L-methionine (SAM) as a methyl donor, regulates various biological processes [10–12]. Coactivator-associated arginine methyltransferase 1 (CARM1/PRMT4) has emerged as a therapeutic target for cancers [13,14] such as breast [15,16], ovarian [17], pancreatic [18], lung [19], and leukemia [20,21]. Notably, CARM1's enzymatic activity is influenced by its post-translational modifications (PTMs), particularly phosphorylation: phosphorylation at the S216 [22], S228 [23,24], S447 [25], and S595 [26] sites affects its SAM binding activity, homodimerization, and subcellular localization. Although CARM1 is primarily localized in the nucleus and functions as a transcriptional regulator, recent studies have increasingly focused on its cytoplasmic functions [27]. Numerous cytoplasmic substrate proteins have been identified, including glyceraldehyde-3-phosphate dehydrogenase [28], pyruvate kinase M2 [29,30], malate dehydrogenase 1 [18], and DRP1 [31], all of which influence energy metabolism and mitochondrial dynamics. Our previous work implicated ROS-mediated cytoplasmic CARM1 localization in mitochondrial fission and senescence *via* DRP1 R403/R634 methylation [31], however, the mechanisms that trigger this localization remain unclear. This study aimed to unravel how reactive oxygen species (ROS) induces CARM1's cytoplasmic localization and to elucidate the role of cytoplasmic CARM1 in cellular senescence and cancer progression.

* Corresponding author. Muscle Physiome Research Center and Research Institute of Pharmaceutical Sciences, Sookmyung Women's University, Seoul, 04310, Republic of Korea.
E-mail address: yksnbk@sookmyung.ac.kr (Y.K. Kim).

https://doi.org/10.1016/j.redox.2024.103344
Received 8 August 2024; Accepted 4 September 2024
Available online 6 September 2024
2213-2317/© 2024 The Authors. Published by Elsevier B.V. This is an open access article under the CC BY-NC-ND license (http://creativecommons.org/licenses/by-nc-nd/4.0/).

2. Methods

2.1. Chemicals, plasmids, and antibodies

Digitonin (D141), 5-dodecanoylaminofluorescein Di-β-D-galactopyranoside (C_{12}FDG, D2893), hydrogen peroxide (386790-M), leptomycin B (L2913), lipopolysaccharide (LPS, L5543), *N*-acetylcysteine (A7250), SB203580 (S8307), SB239063 (S0569), SP600125 (420119), and U0126 (662005) were purchased from Sigma-Aldrich (St. Louis, MO, USA). BIRB 796 (HY-10320), EZM2302 (HY-111109), and TP-064 (HY-114965) were obtained from MedChemExpress (Monmouth Junction, NJ, USA).

HA-CARM1 (#81118) and mCh-DRP1 (#49152) plasmids were purchased from Addgene (Watertown, MA, USA). GFP-CARM1 plasmid was provided by Dr. Mark T. Bedford (University of Texas, MD Anderson Cancer Center, TX, USA). As described previously [31], mCh-DRP1 (R403K, R634K, and R639K) and GFP-CARM1 (E266Q) mutants were generated using the Muta-Direct Site-Directed Mutagenesis Kit (iNtRON Biotechnology, Seongnam, Korea, #15071), following the manufacturer's protocol. HA-CARM1 mutants (S595E and S595A) were produced by BIONICS (Seoul, Korea).

The following antibodies were used for immunoblotting, immunoprecipitation, or immunostaining: Actin (Santa Cruz Biotechnology, Dallas, TX, USA, sc-47778), CARM1 (Bethyl Laboratories, Montgomery, TX, USA, A300-421A), DRP1 (BD Biosciences, Franklin Lakes, NJ, USA, #611113), ERK (Cell Signaling Technology, #9102), phospho-ERK (Cell Signaling Technology, #9101), GFP (Santa Cruz Biotechnology, sc-9996), HA (Cell Signaling Technology, #3724), histone H3 (Cell Signaling Technology, #9715), HSP70/HSP72 (Enzo Life Sciences, Farmingdale, NY, USA, ADI-SPA-810-F), JNK (Cell Signaling Technology, #9258), phospho-JNK (Cell Signaling Technology, #9251), Mff (ProteinTech, Rosemont, IL, 17090-1-AP), OXPHOS (Abcam, Cambridge, UK, ab110411), p16 (Cell Signaling Technology, #29271), p21 (Cell Signaling Technology, #64016, #2947), p38 MAPK (Cell Signaling Technology, #9212), phospho-p38 MAPK (Cell Signaling Technology, #9211), PARP (Santa Cruz Biotechnology, sc-8007), PGC-1α (Santa Cruz Biotechnology, sc-518025), TFAM (Cell Signaling Technology, #8076; Boster Bio, PB9447), TOM20 (ProteinTech, 11802-1-AP; Abnova, H00009804-M01), VDAC1 (Santa Cruz Biotechnology, sc-390996), Alexa Fluor™-conjugated secondary antibodies (Bethyl Laboratories, A90-116D4, A90-138D2, A120-101D4, A120-101F), and HRP-conjugated secondary antibodies (Jackson ImmunoResearch Laboratories, West Grove, PA, USA, #111-035-003, #115-035-003). ADMA[5825] and NFIB antibodies specific for CARM1 substrates were provided by Dr. Mark T. Bedford (University of Texas MD Anderson Cancer Center).

2.2. Cell culture and transfection

MDA-MB-468, BT-20, HCC1143, HCC1806, HCC1937, HCC1395, MDA-MB-231, MCF7, and 10T1/2 cells were obtained from American Type Culture Collection (Manassas, VA, USA). CARM1 WT and KO MEF cells were generously provided by Dr. Mark T. Bedford (University of Texas, MD Anderson Cancer Center). All cells were cultured in RPMI-1640 (HyClone, Logan, UT, USA) or DMEM (HyClone) supplemented with 10 % fetal bovine serum (HyClone) and 100 units/mL penicillin/streptomycin (HyClone). All cells were maintained at 37 °C in a humidified incubator with 5 % CO_2. Transfections were performed using either TransIT®-2020 (Mirus Bio, Madison, Wisconsin, USA, MIR 5400) or TransIT®-X2 (Mirus Bio, MIR 6000), following the manufacturer's instructions.

2.3. Immunofluorescence and confocal microscopy

Cells plated on coverslips were fixed in 4 % paraformaldehyde for 15 min, washed with PBS, and permeabilized with 0.5 % Triton X-100 for 15 min at room temperature. After additional PBS washes, the cells were incubated with a primary antibody overnight at 4 °C, followed by incubation with a secondary antibody conjugated with fluorescein isothiocyanate and/or Alexa Fluor 594. To observe ROS, cells were treated with MitoTracker™ Red CMXRos (100 nM, 1 h) (Thermo Fisher, Waltham, MA, USA) prior to fixation. Immunofluorescence staining was visualized using a Zeiss LSM 710 Confocal Microscope (Carl Zeiss, Oberkochen, Germany) and images were analyzed using ZEN or ImageJ/Fiji software.

2.4. Immunoblotting and immunoprecipitation

Cells were lysed using either NP-40 (10 mM Tris-HCl [pH 7.4], 100 mM NaCl, 1 mM EDTA, 1 mM EGTA, 1 % NP-40, and 10 % glycerol) or RIPA lysis buffer (50 mM Tris-HCl [pH 8], 150 mM NaCl, 0.5 % sodium deoxycholate, 0.1 % sodium dodecyl sulfate, and 1 % Triton X-100) supplemented with a 1 × protease and phosphatase inhibitor cocktail (Roche, Basel, Switzerland). Cells were lysed by sonication, and the lysates were centrifuged at 16,000×*g* for 10 min at 4 °C. Protein concentration was measured using the Bradford assay (Bio-Rad, Hercules, CA, USA) according to the manufacturer's instructions.

For immunoprecipitation, the lysates were adjusted to a concentration of 1 mg/mL and incubated overnight at 4 °C with the appropriate antibodies on a rotator. Protein A/G Sepharose beads (Santa Cruz Biotechnology) were then added and incubated with the lysate for 2 h at 4 °C on a rotator to capture antibody-protein complexes. After washing twice with lysis buffer, the complexes were eluted and separated using sodium dodecyl sulfate-polyacrylamide gel electrophoresis (SDS-PAGE). Proteins were transferred onto polyvinylidene fluoride membranes (Millipore, Billerica, MA, USA), which were blocked with 5 % skim milk/0.1 % Tween 20/Tris-buffered saline for at least 1 h at room temperature. The membrane was then incubated with a primary antibody overnight at 4 °C. After washing thrice with TBS-T, the membrane was incubated with an HRP-linked secondary antibody for 1 h at room temperature. Protein bands were visualized using ECL western blotting substrate (Advansta, Menlo Park, CA, USA).

2.5. Subcellular fractionation

Proteins were extracted from both mitochondrial and cytoplasmic fractions using the Mitochondria/Cytosol Fractionation Kit (BioVision, Milpitas, CA, USA). Cells were gently homogenized in a cytosolic extraction buffer and the homogenate was centrifuged at 700×*g* for 3 min at 4 °C. The supernatant, containing the cytoplasmic fraction, was transferred into a new tube. The pellet was resuspended in RIPA buffer to extract the nuclear fraction. After centrifugation of the supernatant at 10,000×*g* for 30 min at 4 °C, the resulting pellet was resuspended in mitochondrial extraction buffer. Each fraction (cytoplasmic, nuclear, and mitochondrial) was subjected to SDS-PAGE.

2.6. Quantitative real-time PCR

Total cellular RNA was extracted using TRIsure (Bioline, London, UK). Chloroform was added to the cell lysate, followed by vortexing and incubating on ice for 10 min. The mixture was then centrifuged at 16,000×*g* for 15 min at 4 °C. The colorless aqueous phase containing RNA was carefully transferred to a new tube. RNA was precipitated by adding isopropanol, incubated for 10 min at room temperature, and centrifuged at 16,000×*g* for 10 min at 4 °C. The resulting RNA pellet was washed with 70 % ethanol, air-dried, and resuspended in nuclease-free water. cDNA synthesis was performed using the SensiFAST cDNA Synthesis Kit (Bioline). mRNA expression was analyzed using the QuantStudio™ 3 Real-Time PCR System (Applied Biosystems, Foster City, CA, USA) with the SensiFAST™ SYBR No-ROX Kit (Bioline), following the ΔΔCT method. The reaction parameters were as follows: cDNA synthesis at 40 °C for 60 min, transcriptase inactivation at 95 °C for 5 min, and PCR cycling at 95 °C for 10 s, 58 °C for 20 s, and 72 °C for 20 s (40

cycles). The sequences of primer sets were F: ACCTTCTACAATGAGCTGCG and R: CTGGATGGCTACGTACATGG for *Actb*, F: ACCTTCTACAATGAGCTGCG and R: CCTGGATAGCAACGTACATGG for *ACTB*, F: GACATGTTTTCTGACGGCAAC and R: AAGTCCAATGTCCAGCCC for *BAX*, F: GTGGATGACTGAGTACCTGAAC and R: GCCAGGAGAAATCAAACAGAGG for *BCL2*, F: GTTTTCAAGTGCTCGGTGTC and R: CGACAGGTTTTCAGGATGTTG for *Carm1*, F: TTTAAGTGCTCAGTGTCCCG and R: GGCAGGTTTTCAGGATGTTG for *CARM1*, F: TCCCAATTCCATTATCCTCGC and R: CATCAGTACCCGCATCCATG for *Dnm1l*, F: CCACTCACCTCTTCAGAACG and R: CATCTTTGGAAGGTTCAGGTTG for *IL-6*, F: ATACTCCAAACCTTTCCACCC and R: TCTGCACCCAGTTTTCCTTG for *IL-8*, F: CACCAAACCCACAGAAAACAG and R: GGGTCAGAGGAAGAGATAAAGTTG for *Ppargc1a*, F: CACCCAGATGCAAAACTTTCAG and R: CTGCTCTTTATACTTGCTCACAG for *Tfam*.

2.7. Mitochondrial DNA extraction

Genomic DNA was extracted from cultured cells using a DNA Extraction Kit (GeneAll Biotechnology, Seoul, Korea) following the manufacturer's protocol. The DNA was quantified with an Epoch Microplate Spectrophotometer (BioTek, Winooski, VT, USA) and diluted in elution buffer to a final concentration of 200 ng/mL. To assess the relative copy numbers, *16s rRNA* (mitochondrial DNA) and *Hk2* (nuclear DNA) were selected. The sequences of the primer sets were F: CCGCAAGGGAAAGATGAAAGAC and R: TCGTTTGGTTTCGGGGTTTC for 16s *rRNA* and F: GCCAGCCTCTCCTGATTTTAGTGT and R: GGGAACACAAAAGACCTCTTCTGG for *Hk2*.

2.8. Site-directed mutagenesis

The PCR product generated with mutagenic primers was amplified using Pfu polymerase and digested with *Dpn*I to eliminate methylated plasmid DNA. Subsequently, it was introduced into competent *E. coli* DH5α cells (Enzynomics, Daegeon, Korea). The transformed cells were then spread onto Luria-Bertani agar plates supplemented with ampicillin or kanamycin for selection. Mutant plasmids were extracted using either the FavorPrep™ Plasmid Extraction Mini Kit (Favorgen, Wien, Austria) or the Fast Ion Plasmid Midi Kit (RBC Bioscience, New Taipei City, Taiwan).

2.9. Senescence-associated β-galactosidase assay

β-galactosidase activity was assessed following established methods [32]. Cells were washed with PBS, fixed at room temperature for 15 min, and then incubated overnight at 37 °C (no CO_2) for β-galactosidase staining using the Senescence β-Galactosidase Staining Kit (Cell Signaling Technology, #9860), following the manufacturer's instructions. Blue-stained cells were counted under a light microscope to quantify the senescent cells. For fluorescence-based quantification, cells were treated with bafilomycin A1 (100 nM, 1 h) and then incubated with 5-dodecanoylaminofluorescein Di-β-D-galactopyranoside (C_{12}FDG; 33 μM, 1 h), a green fluorescence substrate for β-galactosidase detection. After trypsinization, the cells were resuspended in cold PBS containing 0.5 % bovine serum albumin (BSA). Data analysis was performed using the FlowJo software (https://www.flowjo.com/solutions/flowjo/).

2.10. EdU incorporation assay

Cell proliferation rates were evaluated using the EdU Proliferation Kit (Abcam, ab219801). Cells were seeded, pulse-labeled with 20 μM EdU for 3 h, and harvested by trypsinization. The harvested cells were washed with a 3 % BSA solution in PBS, fixed with 4 % formaldehyde for 15 min in the dark, and permeabilized. Subsequently, cells were treated with an EdU reaction mixture containing $CuSO_4$, iFluor® 488 azide, and sodium ascorbate for 30 min at room temperature in the dark. After washing, the samples were transferred into fresh tubes on ice. Fluorescence intensity was measured using a FACSCalibur™ system, and data were analyzed using FlowJo software.

2.11. Cell counting, colony forming, and MTT assays

Cell growth and viability were assessed using cell counting, colony forming, and MTT assays. For cell counting, cells were seeded in 12-well plates at a density of 10,000 cells/well and treated with EZM2302 the following day. After 24, 48, and 72 h, the cells were harvested using trypsin and counted using a Z2 Coulter Counter (Beckman Coulter, Brea, CA, USA). The counted cells had diameters ranging from 10 to 30 μm.

For the colony forming assay, cells were seeded in 6-well plates at a density of 1000 cells/well and treated with CARM1 siRNA, EZM2302, or TP-064 for 72 h. Colonies were fixed with 4 % paraformaldehyde, stained with 0.05 % crystal violet, washed with deionized water, and air-dried. The stained crystal violet was dissolved in 30 % acetic acid solution, and the absorbance at 540 nm was measured using an Epoch Microplate Spectrophotometer.

For the MTT assay, cells seeded in 96-well plates were treated with varying concentrations of EZM2302 or TP-064 for 48 h. Following treatment, 0.5 mg/mL MTT solution was added to each well and incubated for 2 h. The media was then discarded, and 120 μL of DMSO was added to solubilize formazan crystals. Absorbance was measured at 590 nm using an Epoch Microplate Spectrophotometer.

2.12. Statistical analysis

Statistical analyses were conducted using Prism software (GraphPad). Data represent independent experiments and are presented as mean ± standard deviation ($n \geq 3$). Comparisons between two groups were assessed using unpaired t-tests for independent samples. Statistical significance was defined as $p < 0.05$; *$p < 0.05$, **$p < 0.01$, and ***$p < 0.001$ indicate significance levels.

3. Results

3.1. Subcellular localization of CARM1 determines the mitochondrial morphology and quantity

To differentiate the functions of CARM1 between the nucleus and the cytoplasm, we first examined its subcellular localization in various cell lines. Given the upregulation of CARM1 expression in breast cancer and its association with high-grade tumors [33], we evaluated CARM1 levels in the triple-negative breast cancer (TNBC) cell lines: MDA-MB-468, BT-20, HCC1143, HCC1806, HCC1937, HCC1395, and MDA-MB-231. The total levels of CARM1 were notably elevated in HCC1395 and MDA-MB-231 cells, representatives of more aggressive TNBC B subtype (Supplementary Fig. 1A). Additionally, the cytoplasmic levels of CARM1 were also elevated (Fig. 1A–C). We obtained spontaneously transformed 10T1/2 (t10T1/2) cells from a non-tumorigenic 10T1/2 mouse embryo fibroblast (MEF) cell line, which exhibited distinct characteristics, such as irregular cell morphology, colony-forming ability, anchorage-independent growth, and alterations in chromatin structure (Supplementary Figs. 1B–E). Interestingly, we observed a dramatic shift in the subcellular localization of CARM1 from the nucleus to the cytoplasm in t10T1/2 cells (Fig. 1D and E). These findings suggest that cellular functions could be influenced by the subcellular localization of CARM1, implying its potential involvement in the regulation of cancer progression or cellular transformation. Consistent with our previous findings that cytoplasmic CARM1 induces mitochondrial fission through DRP1 methylation [31], we observed an increase in fragmented mitochondria (Fig. 1D), mitochondrial recruitment of DRP1 (Fig. 1E), and ROS levels (Fig. 1F) in t10T1/2 cells. Remarkably, t10T1/2 cells exhibited increased mitochondrial mass, as evidenced by the elevated levels of mtDNA (Fig. 1G), translocase of outer mitochondrial membrane

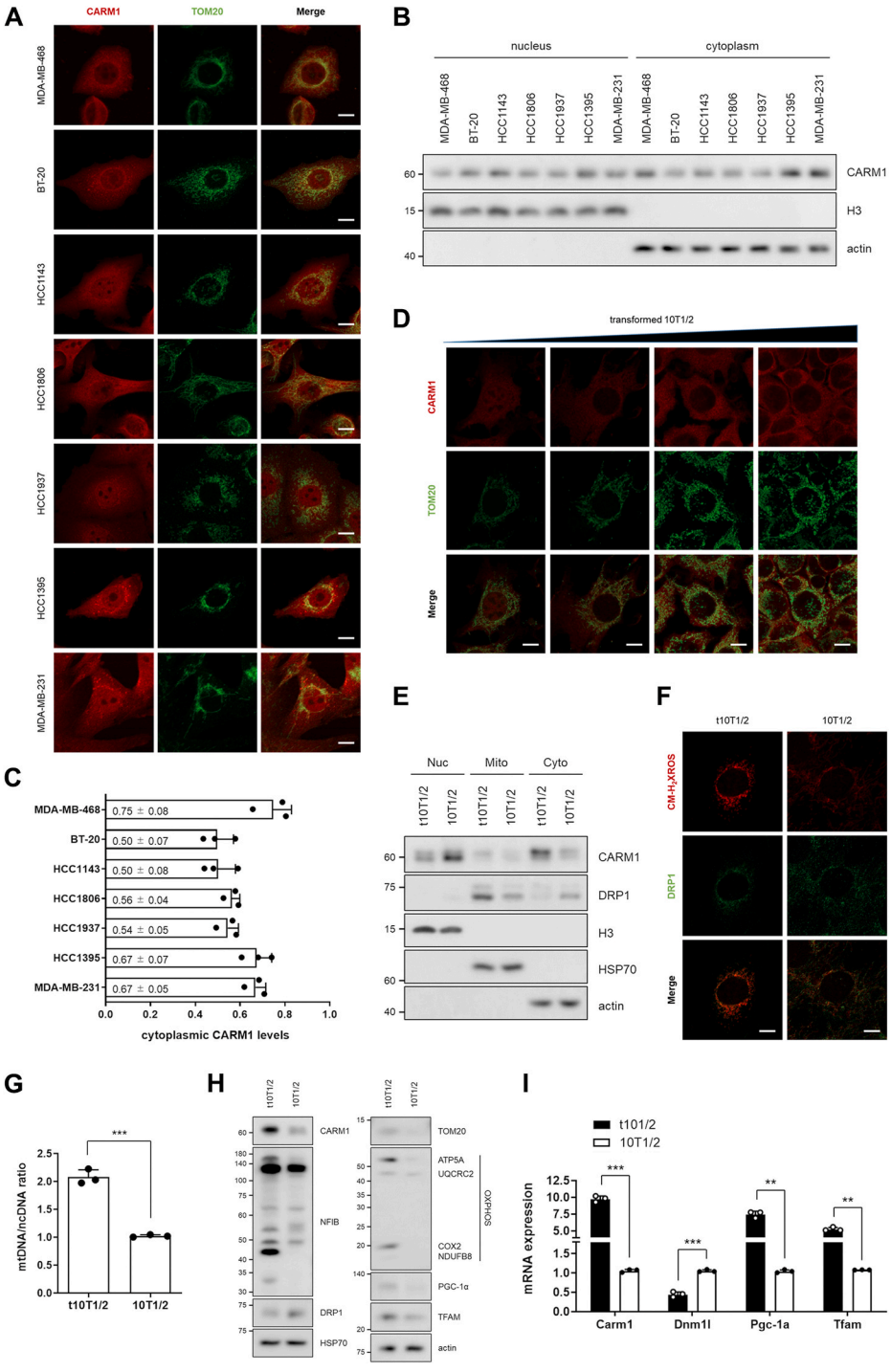

Fig. 1. Cytoplasmic CARM1 determines the morphology and quantity of mitochondria.
(**A-C**) Double immunostaining for CARM1 (red) and TOM20 (green), scale bars, 10 μm (**A**), western blots of the nuclear and cytoplasmic fractions (**B**), and relative cytoplasmic CARM1 levels (**C**) in triple-negative breast cancer cell lines (MDA-MB-468, BT-20, HCC1143, HCC1806, HCC1937, HCC1395, and MDA-MB-231). (**D**) Double immunostaining for TOM20 (green) and CARM1 (red) in transformed 10T1/2 cells. Scale bars, 10 μm. (**E**) Western blots of the nuclear, mitochondrial, and cytoplasmic fractions from transformed or parental 10T1/2 cells. (**F**) Confocal images of MitoTracker™ CM-H_2XROS (red) and DRP1 (green) in transformed or parental 10T1/2 cells. Scale bars, 10 μm. (**G-I**) mtDNA/ncDNA, measured using quantitative real-time PCR (**G**), western blots of cell lysates (**H**), and mRNA expression levels (**I**) from transformed or parental 10T1/2 cells. Error bars represent mean ± SD ($n = 3$). (For interpretation of the references to color in this figure legend, the reader is referred to the Web version of this article.)

complex subunit 20 (TOM20), and oxidative phosphorylation (OXPHOS) proteins (Fig. 1H). This increase was attributed to the upregulation of *Pgc-1α* and *Tfam*, master regulators of mitochondrial biogenesis [7,8] (Fig. 1H and I). These findings underscore the role of CARM1 subcellular localization in determining both mitochondrial biogenesis and dynamics.

3.2. Nuclear CARM1 limits mitochondrial biogenesis by suppressing PGC-1α expression

To investigate how CARM1 influences mitochondrial biogenesis and dynamics, we first measured the mitochondrial quantity in CARM1 wild-type (WT) and knockout (KO) MEF cells. There was a significant increase in mtDNA (Fig. 2A), TOM20 (Fig. 2B and C), and OXPHOS proteins (Fig. 2C) in CARM1 KO MEF cells, indicating that CARM1 negatively regulates mitochondrial quantity. Additionally, we observed elevated mRNA and protein levels of PGC-1α in CARM1 KO MEF cells (Fig. 2D and E). This increase in PGC-1α levels decreased upon the introduction of CARM1 WT, but not its enzyme-dead mutant E266Q, into CARM1 KO MEF cells (Fig. 2E). These findings were consistently observed in 10T1/2 cells subjected to transient knockdown (KD) or inhibition of CARM1 using small interfering RNA (siRNA) or the selective inhibitor EZM2302 [34] (Supplementary Figs. 2A–F). All these data support the idea that nuclear CARM1 limits mitochondrial biogenesis by suppressing PGC-1α. Further supporting this notion, higher levels of TOM20 and OXPHOS proteins were present in MCF7 cells than in normal fibroblasts (Fig. 2G and H), accompanied by lower nuclear CARM1 levels in MCF7 cells (Fig. 2F).

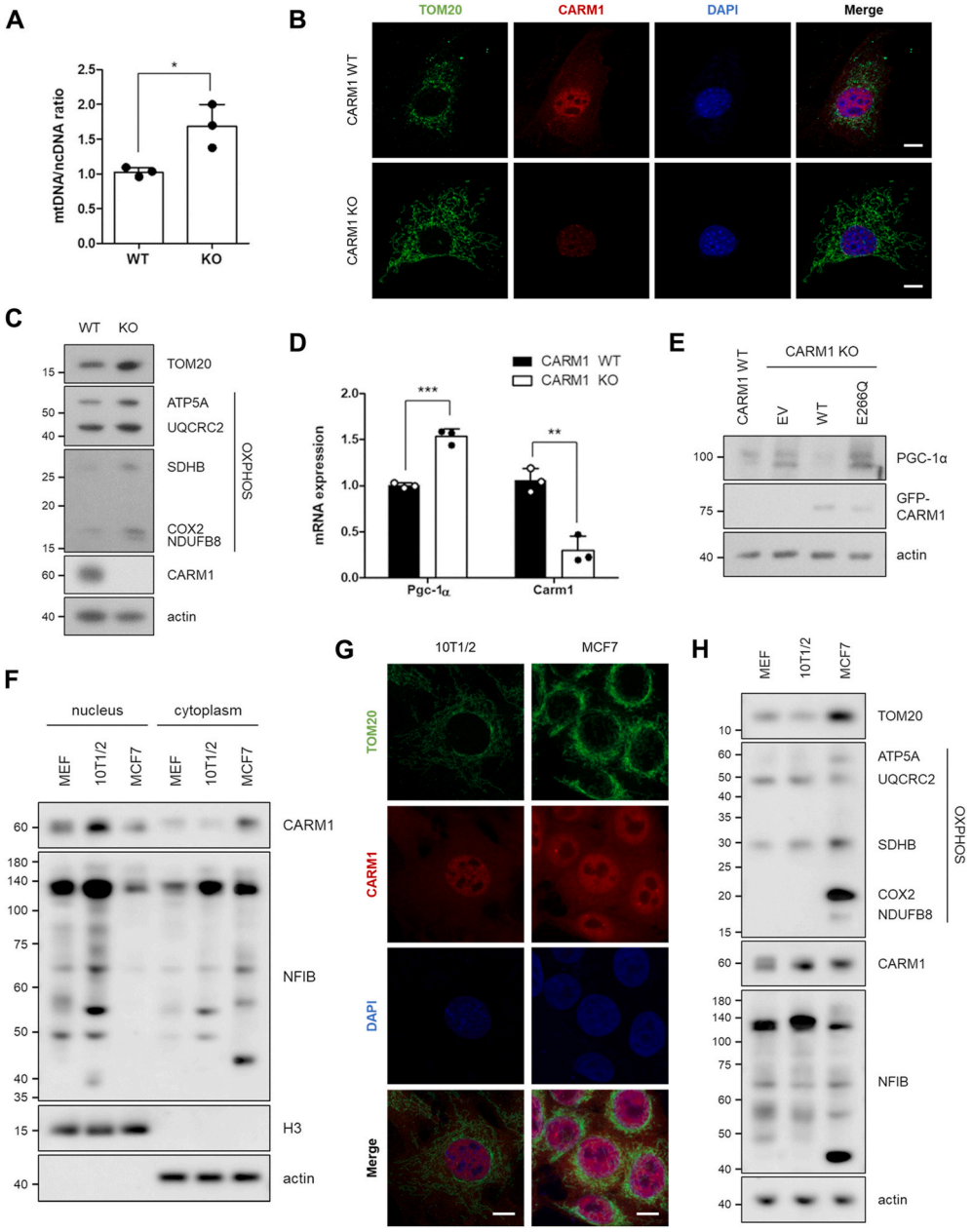

Fig. 2. Nuclear CARM1 limits mitochondrial biogenesis by suppressing PGC-1α and TFAM.
(**A**) mtDNA/ncDNA, measured through quantitative real-time PCR in CARM1-WT or -KO MEF cells. Error bars represent mean ± SD ($n = 3$). (**B**) Confocal images of TOM20 (green), CARM1 (red), and DAPI (blue) in CARM1-WT or -KO MEF cells. Scale bars, 10 μm. (**C**) Western blots of cell lysates from CARM1-WT or -KO MEF cells. The protein levels of TOM20 and OXPHOS are reliable markers of mitochondrial mass. (**D**) mRNA expression levels of *Pgc-1α* and *Carm1* in CARM1-WT or -KO MEF cells. Error bars represent mean ± SD ($n = 3$). (**E**) Western blots of cell lysates from CARM1-WT or -KO MEF cells transfected with GFP-CARM1 (WT or E266Q) for 48 h. (**F**) Western blots of the nuclear and cytoplasmic fractions from MEF, 10T1/2, or MCF7 cells. (**G**) Confocal images of TOM20 (green), CARM1 (red), and DAPI (blue) in 10T1/2 or MCF7 cells. Scale bars, 10 μm. (**H**) Western blots of cell lysates from MEF, 10T1/2, or MCF7 cells. (For interpretation of the references to color in this figure legend, the reader is referred to the Web version of this article.)

3.3. Cytoplasmic translocation of CARM1 requires p38γ MAPK activation by ROS

Interestingly, we noted not only higher expression levels of CARM1 but also a band shift in t10T1/2 and MCF7 cells (Figs. 1H and 2H). Given that cancer cells typically have elevated basal ROS levels compared with normal cells [35], we first explored the ROS-activated MAPK signaling pathways, including p38, ERK, and JNK [36], to investigate the possibility of a band shift of CARM1 caused by phosphorylation. As expected, the phosphorylation of p38 MAPK, but not that of other MAPKs, was substantially increased in t10T1/2 and MCF7 cells (Supplementary Figs. 3A and B). ROS signaling has been reported to translocate CARM1 to the cytoplasm in a CRM1 (chromosomal maintenance 1)-dependent manner [31], which was further corroborated by our observation that lipopolysaccharide (LPS) induces ROS production and enriches cytoplasmic CARM1 (Supplementary Fig. 3C). Additionally, a recent report suggested that phosphorylation of CARM1 at S595 by p38γ MAPK contributes to its cytoplasmic translocation [26]. Thus, we hypothesized that ROS-induced p38 MAPK signaling phosphorylates CARM1, facilitating its translocation into the cytoplasm. Indeed, treatment with LPS or H_2O_2 led to increased phosphorylation of p38 MAPK and a band shift in CARM1, both of which were mitigated by *N*-acetylcysteine (NAC) (Fig. 3A and B), but not by leptomycin B (LMB), a specific nuclear export inhibitor (Fig. 3C and D). The observed band shift of CARM1 upon cotreatment with H_2O_2 and LMB was exclusively confined to the nucleus (Fig. 3D), indicating that ROS-activated p38 MAPK phosphorylated CARM1 and subsequently exported phosphorylated CARM1 from the nucleus in a CRM1-dependent manner. To validate the involvement of p38γ MAPK, we conducted an experiment utilizing MAPK isoform-specific inhibitors targeting p38α/β (SB203580 and SB239063), pan-p38 (BIRB 796), ERK (U0126), and JNK (SP600125). Remarkably, only BIRB 796 inhibited the band shift and cytoplasmic localization of CARM1 induced by ROS (Fig. 3E–H and Supplementary Figs. 3D–F), consequently suppressing mitochondrial recruitment of DRP1 and fission (Fig. 3H and I). These findings underscore the role of p38γ MAPK in phosphorylating CARM1 and facilitating its cytoplasmic translocation.

3.4. p38γ MAPK phosphorylates CARM1 at S595, triggering cellular senescence

To validate the significance of CARM1 S595 phosphorylation by p38γ MAPK in cytoplasmic translocation and subsequent intracellular functions, we generated mutant forms of CARM1 in which S595 was substituted with E (phosphomimetic) or A (phospho-deficient). LPS treatment did not induce a band shift in the S595A mutant (Fig. 4A), supporting that ROS-activated p38γ MAPK phosphorylates CARM1 at S595. Moreover, unlike the S595A mutant, S595E not only showed enrichment but also significantly increased methylation levels of its substrate proteins in the cytoplasm (Fig. 4B and Supplementary Fig. 4A), suggesting that S595 phosphorylation facilitates its translocation to the cytoplasm and regulates its cytoplasmic functions. Indeed, the S595E mutant showed elevated DRP1 methylation (Supplementary Fig. 4B) and its mitochondrial recruitment (Supplementary Fig. 4C), thereby enhancing mitochondrial fission (Fig. 4C and D). Through these processes, the S595E mutant promoted intracellular ROS generation (Fig. 4E) and cellular senescence (Fig. 4F–J and Supplementary Figs. 4D and E). Specifically, overexpression of the S595E mutant increased cellular senescence markers, including the mRNA levels of senescence-associated secretory phenotype (SASP) factors, interleukin (IL)-6 and IL-8 (Fig. 4F), the percentage of β-galactosidase-positive cells (Fig. 4G), and p21 expression (Fig. 4H and Supplementary Fig. 4D), accompanied by G1 phase arrest (Supplementary Fig. 4E). This effect of the S595E mutant overexpression became more pronounced under cellular senescence conditions induced by H_2O_2 (Fig. 4H–J), supporting the notion that phosphorylation of CARM1 at S595 accelerates cellular senescence *via* DRP1 methylation. To further clarify that ROS-mediated cellular senescence depends on CARM1-DRP1 axis, we performed the experiment using DRP1 methylation-deficient mutants (R403K and R634K) after depleting endogenous CARM1 and DRP1. As expected, CARM1 S595E did not increase p16 and p21 levels in either DRP1 knocked down or methylation-deficient mutant-expressing cells (Supplementary Fig. 4F).

3.5. Inhibition of CARM1 promotes the apoptotic death of senescent cells

Given our findings that cytoplasmic CARM1 levels increased due to phosphorylation at S595 by ROS-activated p38γ MAPK in both cancer and senescent cells, we investigated whether inhibiting CARM1 would have distinct effects on cell growth depending on its localization. CARM1 selective inhibitors, EZM2302 [34] and TP-064 [37], showed anti-proliferative effects in cancer cells but not in normal cells. This was evidenced by the EdU incorporation (Fig. 5A and Supplementary Fig. 5A), colony-forming (Fig. 5B, C and Supplementary Figs. 5B and C), MTT assays (Fig. 5D, E and Supplementary Fig. 5D), and cell counting (Fig. 5F and Supplementary Fig. 5E). Furthermore, after inducing cellular senescence, EZM2302 treatment significantly reduced the percentage of β-galactosidase-positive cells (Fig. 5G and H), as well as the levels of p21 and SASP factors (Fig. 5I and J). Additionally, we observed poly (ADP-ribose) polymerase cleavage due to caspase-3 activation and an increase in the *BAX/BCL2* ratio in senescent cells treated with EZM2302 (Fig. 5I–K). These results suggested that EZM2302 eliminates senescent cells through apoptosis and functions as a senolytics. Taken together, cancer and senescent cells exhibiting elevated cytoplasmic CARM1 levels (Fig. 1B–E, 2F and Supplementary Fig. 5F) were sensitive to CARM1 inhibitors, indicating that targeting cytoplasmic CARM1 could be a novel approach for treating cancer and senescent cells.

4. Discussion

Although the nuclear functions of PRMTs, such as cell cycle regulation [11], DNA repair [12], and transcription [38], are well established, their cytoplasmic roles are emerging as crucial for maintaining cellular homeostasis. Among these PRMTs, CARM1 methylates cytoplasmic substrate proteins, thereby participating in various metabolic processes, including glycolysis, oxidative phosphorylation, and glutamine metabolism [18,28–30]. Additionally, our recent report highlights CARM1's pivotal role in regulating mitochondrial dynamics, emphasizing its cytoplasmic functions [31]. In this paper, we provide clear evidence of how the nuclear-cytoplasmic shuttling of CARM1 cooperatively regulates mitochondrial homeostasis and elucidate the signaling pathways mediating its cytoplasmic localization. Specifically, in a resting state, nuclear CARM1 suppresses the transcription of *PGC-1α* and *TFAM*, resulting in decreased mitochondrial biogenesis, while concurrently increasing *DNM1L* transcription to regulate mitochondrial fission. Our study showed that excessive stimuli, such as ROS, activate p38γ MAPK, which triggers CARM1 shuttling through phosphorylation at S595. In the cytoplasm, CARM1 directly methylates DRP1, inducing mitochondrial fission and ROS production. This ROS-mediated positive feedback loop further enhances cytoplasmic CARM1 localization, contributing to mitochondrial dysregulation and cellular senescence. Meanwhile, in the nucleus, DRP1 expression is reduced due to decrease in nuclear CARM1 levels [31]. Although we cannot provide a comprehensive explanation for this response, it is possible that it plays as a protective mechanism to mitigate the vicious cycle of ROS-CARM1-DRP1 triggered by strong stress stimuli. Once exposed to stimuli exceeding this protective mechanism, it may lead to pathological conditions such as cellular senescence. Supporting this notion, our findings indicated that in both senescent and transformed cells, CARM1 localizes substantially to the cytoplasm, coinciding with an increase in fragmented mitochondria (Figs. 1D and 4C).

Recent research has focused on splicing variants of CARM1 [39,40].

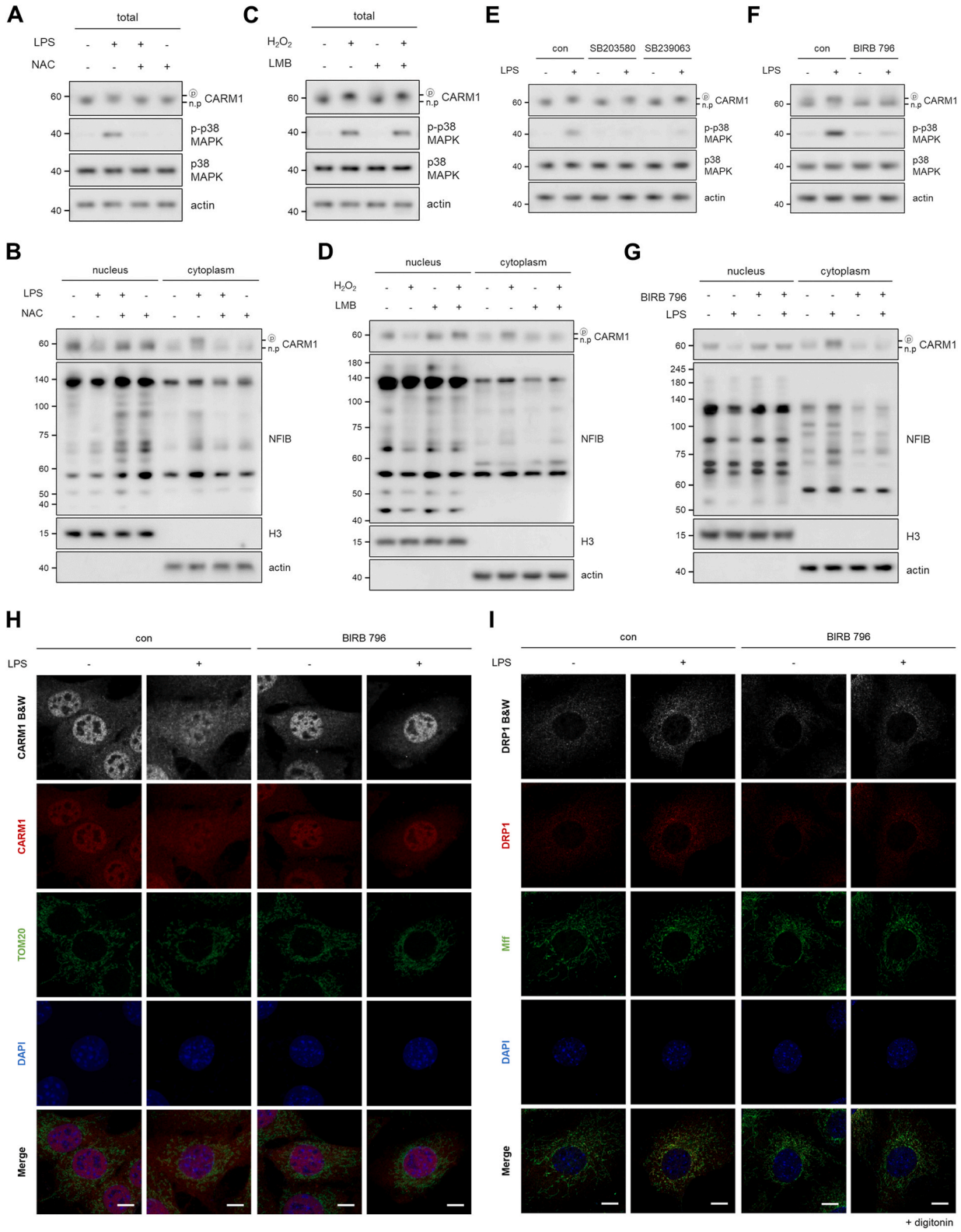

Fig. 3. Cytoplasmic translocation of CARM1 requires p38γ MAPK activation by ROS.
(**A,B**) Western blots of total lysates (**A**) and nuclear/cytoplasmic fractions (**B**) from 10T1/2 cells treated with 100 ng/mL LPS or/and 10 mM NAC for 3 h. (**C,D**) Western blots of total lysates (**C**) and nuclear/cytoplasmic fractions (**D**) from 10T1/2 cells treated with 0.5 mM H_2O_2 or/and 10 nM LMB for 3 h. (**E,F**) Western blots of cell lysates from 10T1/2 cells pre-treated with p38 MAPK inhibitor (SB203580, SB239063, or BIRB 796) at 10 μM for 1 h prior to LPS stimulation. (**G-I**) Western blots of the nuclear and cytoplasmic fractions (**G**), double immunostaining for CARM1 (red) and TOM20 (**H**), and for DRP1 (red), Mff (green) (**I**) from 10T1/2 cells pre-treated with BIRB 796 prior to LPS stimulation. Digitonin (20 μg/mL, 2 min) was used for treatment before fixation to remove the cytoplasmic DRP1. Scale bars, 10 μm. (For interpretation of the references to color in this figure legend, the reader is referred to the Web version of this article.)

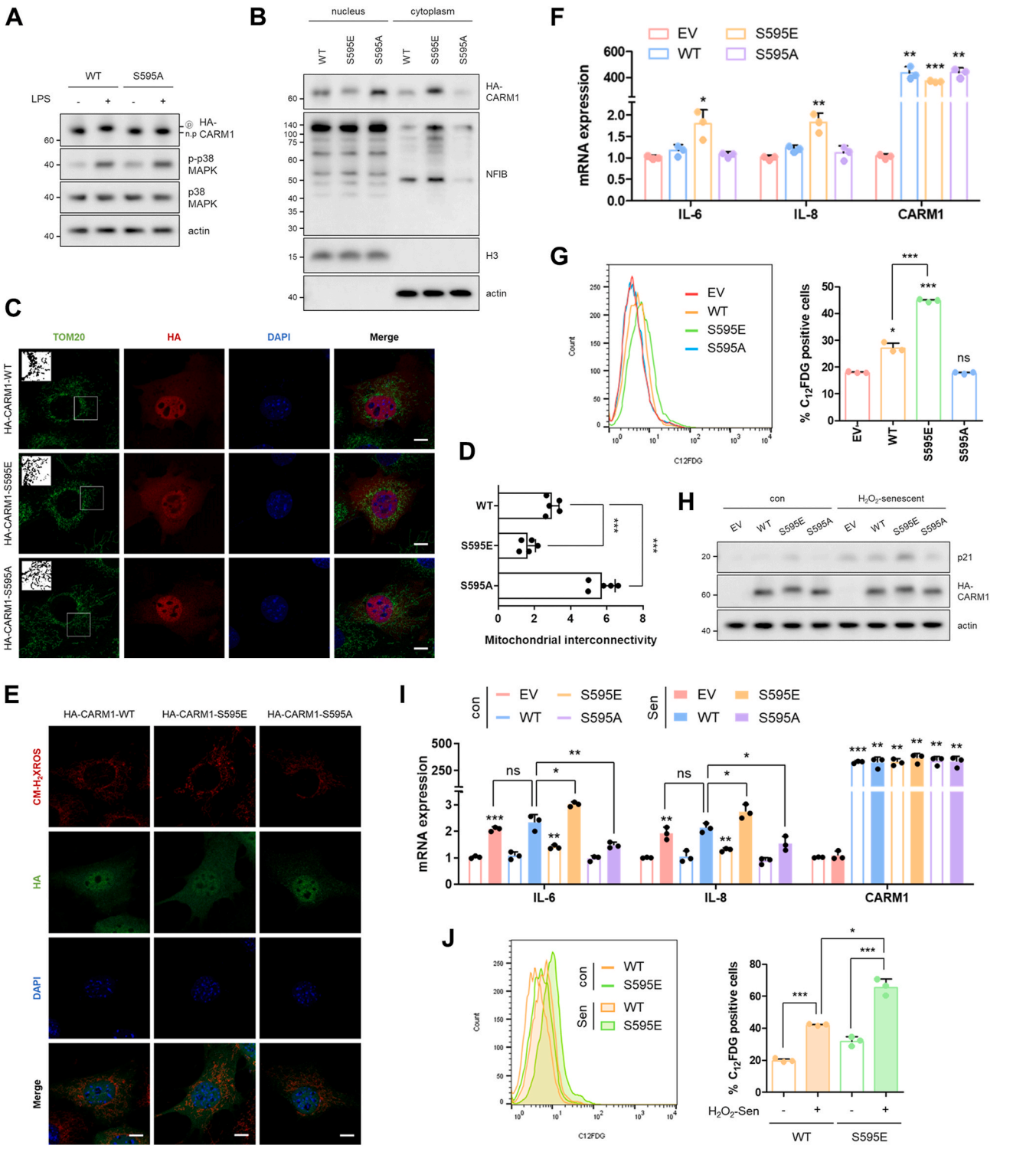

Fig. 4. p38γ MAPK phosphorylates CARM1 at S595, triggering cellular senescence.
(**A**) Western blots of cell lysates from 10T1/2 cells transfected with HA-CARM1 (WT or S595A) for 48 h and then treated with LPS (100 ng/mL, 3 h). (**B**) Western blots of the nuclear and cytoplasmic fractions from 10T1/2 cells transfected with HA-CARM1 (WT, S595E, or S595A) for 48 h. (**C,D**) Confocal images of TOM20 (green) and HA (red) from 10T1/2 cells overexpressing HA-CARM1 (WT, S595E, or S595A). Scale bars, 10 μm. Mitochondrial morphology was analyzed using ImageJ/FiJi software. The more fragmented the mitochondria, the lower the mitochondrial interconnectivity. Data are presented as mean ± SD ($n = 5$). (**E**) Confocal images of MitoTracker™ CM-H_2XROS (red) and HA (green) from 10T1/2 cells overexpressing HA-CARM1 (WT, S595E, or S595A). Scale bars, 10 μm. (**F,G**) mRNA expression levels of SASP factors (**F**) and β-galactosidase activity assessed using its fluorescent substrate C_{12}FDG (**G**) from the cells transfected with HA-CARM1 (WT, S595E, or S595A) for 48 h. Error bars indicate mean ± SD ($n = 3$). (**H-J**) p21 protein levels (**H**), mRNA expression levels of SASP factors (**I**), and β-galactosidase activity (**J**) upon senescence induction (0.5 mM H_2O_2 for 3 h and then fresh media for 24 h) in cells overexpressing HA-CARM1 WT or mutant. Error bars represent mean ± SD ($n = 3$). (For interpretation of the references to color in this figure legend, the reader is referred to the Web version of this article.)

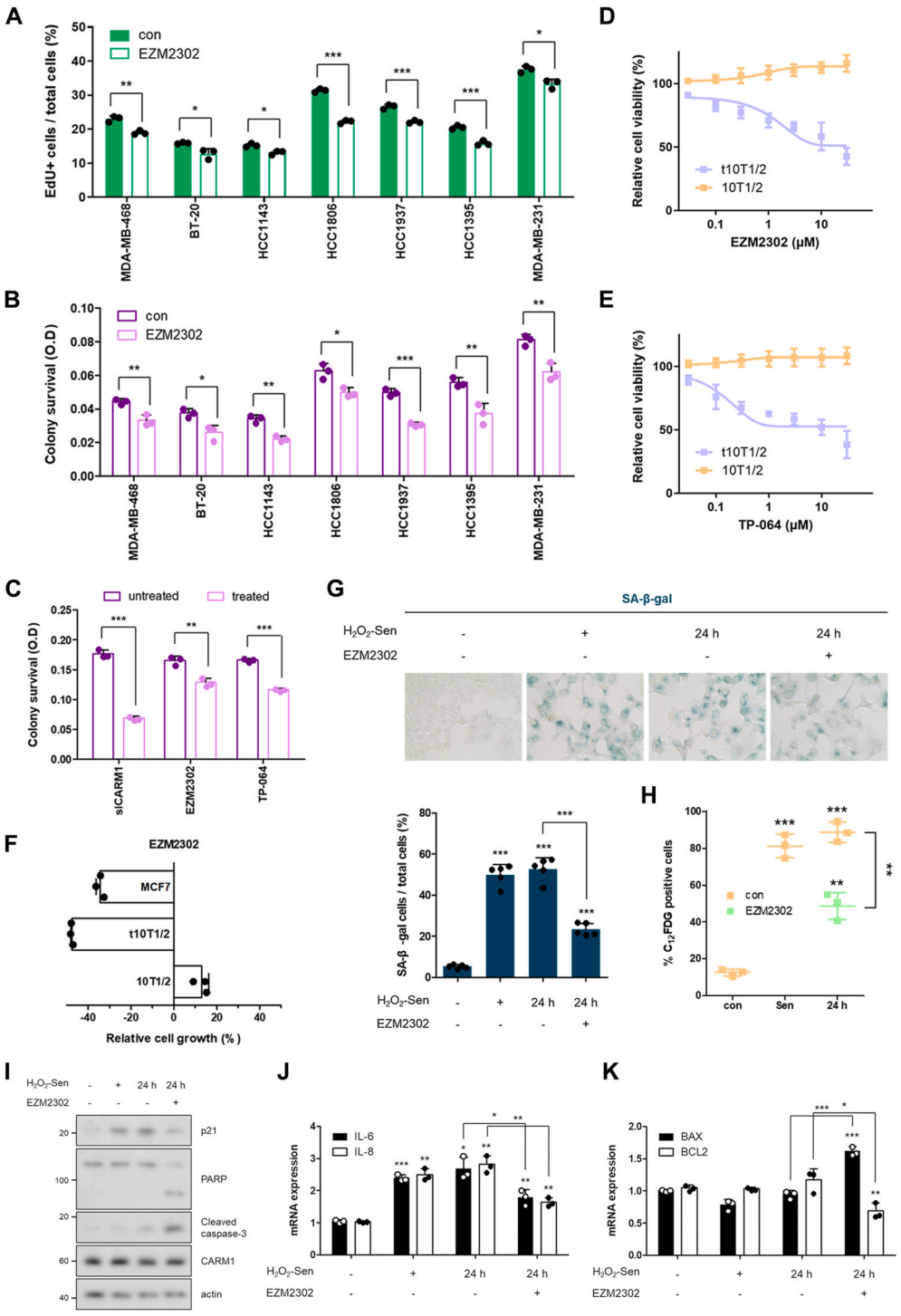

Fig. 5. Inhibition of CARM1 promotes the apoptotic death of senescent cells.
(**A,B**) EdU incorporation assay (**A**) and colony forming assay (**B**) in triple-negative breast cancer cell lines treated with EZM2302 (1 μM, 72 h). EdU was incubated at 20 μM for 3 h and EdU positive cells were counted using flow cytometry. Colonies were stained with crystal violet and absorbance was measured at 540 nm. Error bars represent mean ± SD ($n = 3$). (**C**) Colony forming assay in transformed 10T1/2 cells treated with CARM1 siRNA, EZM2302 (1 μM), or TP-064 (1 μM) for 72 h. Error bars indicate mean ± SD ($n = 3$). (**D,E**) The effects of EZM2302 (**D**) or TP-064 (**E**) on cell growth in transformed or parental 10T1/2 cells. (**F**) Relative cell growth percentage upon EZM2302 treatment in MCF7, transformed, or parental 10T1/2 cells. (**G**) Representative images of SA-β-gal assay. After induction of senescence, EZM2302 was treated at 1 μM for 24 h. Data are presented as mean ± SD ($n = 5$). (**H–K**) β-galactosidase activity (**H**), western blots of cell lysates (**I**), and mRNA expression levels (**J,K**) from MCF7 cells treated with 1 μM EZM2302 for 24 h, after senescence induction. Error bars indicate mean ± SD ($n = 3$). (For interpretation of the references to color in this figure legend, the reader is referred to the Web version of this article.)

Similar to full-length CARM1 (CARM1-FL), the truncated form lacking exon 15 (CARM1-ΔE15) is highly expressed in breast [39] and hematopoietic [20] cell lines, forming homo- and heterodimers [39]. Overexpression of CARM1-FL (but not CARM1-ΔE15) or KO of all CARM1 isoforms, impedes the proliferation of cancer cells primarily expressing CARM1-ΔE15 [40,41], suggesting an oncogenic role for CARM1-ΔE15. These variants exhibit differential subcellular localization: predominantly nuclear for CARM1-FL and potentially cytoplasmic for CARM1-ΔE15 [40]. This indicates that the cytoplasmic enrichment of CARM1 could potentially induce cellular transformation or cancer progression, which is supported by our findings that ROS-mediated p38γ MAPK facilitates CARM1 translocation to the cytoplasm. Cytoplasmic CARM1 methylates various substrate proteins, including DRP1, enhancing ROS production and promoting cellular transformation.

In summary, we have demonstrated the nuclear functions of CARM1 in maintaining mitochondrial homeostasis by influencing *PGC-1α*, *TFAM*, and *DNM1L* transcription, thereby regulating mitochondrial biogenesis and dynamics. Under oxidative stress conditions, p38γ MAPK activation phosphorylates CARM1 at S595, promoting its cytoplasmic localization without changing its enzymatic activity. Increased cytoplasmic CARM1 levels induce mitochondrial fission by methylating DRP1, which leads to ROS-mediated cellular senescence. Further exploration of cytoplasmic CARM1 functions is warranted; however, our findings suggest that the developing cytoplasmic CARM1 selective inhibitor may offer novel strategies for anti-cancer or anti-aging therapies.

CRediT authorship contribution statement

Yena Cho: Conceptualization, Data curation, Formal analysis, Investigation, Writing – original draft, Writing – review & editing. **Yong Kee Kim:** Conceptualization, Formal analysis, Funding acquisition, Supervision, Writing – original draft, Writing – review & editing.

Declaration of competing interest

The authors declare that they have no known competing financial interests or personal relationships that could have appeared to influence the work reported in this paper.

Data availability

Supplementary information is available for this paper. All other data supporting the findings of this study are available from the corresponding author upon request.

Acknowledgements

This study was supported by grants from the National Research Foundation of Korea (NRF) and Korean government (MSIT) (2022R1A5A2021216 and 2021R1A2C2013613 to Y.K.K., respectively).

Appendix A. Supplementary data

Supplementary data to this article can be found online at https://doi.org/10.1016/j.redox.2024.103344.

References

[1] H. Vakifahmetoglu-Norberg, A.T. Ouchida, E. Norberg, The role of mitochondria in metabolism and cell death, Biochem. Biophys. Res. Commun. 482 (2017) 426–431, https://doi.org/10.1016/j.bbrc.2016.11.088.
[2] C. Wang, R.J. Youle, The role of mitochondria in apoptosis, Annu. Rev. Genet. 43 (2009) 95–118, https://doi.org/10.1146/annurev-genet-102108-134850.
[3] O. Matilainen, P.M. Quiros, J. Auwerx, Mitochondria and epigenetics - crosstalk in homeostasis and stress, Trends Cell Biol. 27 (2017) 453–463, https://doi.org/10.1016/j.tcb.2017.02.004.
[4] A.M. van der Bliek, M.M. Sedensky, P.G. Morgan, Cell biology of the mitochondrion, Genetics 207 (2017) 843–871, https://doi.org/10.1534/genetics.117.300262.
[5] F.R. Jornayvaz, G.I. Shulman, Regulation of mitochondrial biogenesis, Essays Biochem. 47 (2010) 69–84, https://doi.org/10.1042/bse0470069.
[6] L. Tilokani, S. Nagashima, V. Paupe, J. Prudent, Mitochondrial dynamics: overview of molecular mechanisms, Essays Biochem. 62 (2018) 341–360, https://doi.org/10.1042/EBC20170104.
[7] P. Puigserver, Z. Wu, C.W. Park, R. Graves, M. Wright, B.M. Spiegelman, A cold-inducible coactivator of nuclear receptors linked to adaptive thermogenesis, Cell 92 (1998) 829–839, https://doi.org/10.1016/s0092-8674(00)81410-5.
[8] J.V. Virbasius, R.C. Scarpulla, Activation of the human mitochondrial transcription factor A gene by nuclear respiratory factors: a potential regulatory link between nuclear and mitochondrial gene expression in organelle biogenesis, Proc. Natl. Acad. Sci. U.S.A. 91 (1994) 1309–1313, https://doi.org/10.1073/pnas.91.4.1309.
[9] H. Martini, J.F. Passos, Cellular senescence: all roads lead to mitochondria, FEBS J. 290 (2023) 1186–1202, https://doi.org/10.1111/febs.16361.
[10] J.W. Hwang, Y. Cho, G. Bae, S. Kim, Y.K. Kim, Protein arginine methyltransferases: promising targets for cancer therapy, Exp. Mol. Med. 53 (2021) 788–808, https://doi.org/10.1038/s12276-021-00613-y.
[11] S. Kim, N.H. Kim, J.E. Park, J.W. Hwang, N. Myung, K. Hwang, Y.A. Kim, C. Jang, Y.K. Kim, PRMT6-mediated H3R2me2a guides aurora B to chromosome arms for proper chromosome segregation, Nat. Commun. 11 (2020) 612–w, https://doi.org/10.1038/s41467-020-14511-w.
[12] J.W. Hwang, S. Kim, N. Myung, D. Song, G. Han, G. Bae, M.T. Bedford, Y.K. Kim, PRMT5 promotes DNA repair through methylation of 53BP1 and is regulated by src-mediated phosphorylation, Commun. Biol. 3 (2020) 428–z, https://doi.org/10.1038/s42003-020-01157-z.
[13] Z. Xie, Y. Tian, X. Guo, N. Xie, The emerging role of CARM1 in cancer, Cell. Oncol. (2024), https://doi.org/10.1007/s13402-024-00943-9.
[14] M. Santos, J.W. Hwang, M.T. Bedford, CARM1 arginine methyltransferase as a therapeutic target for cancer, J. Biol. Chem. 299 (2023) 105124, https://doi.org/10.1016/j.jbc.2023.105124.
[15] S. Frietze, M. Lupien, P.A. Silver, M. Brown, CARM1 regulates estrogen-stimulated breast cancer growth through up-regulation of E2F1, Cancer Res. 68 (2008) 301–306, https://doi.org/10.1158/0008-5472.CAN-07-1983.
[16] H.O. Habashy, E.A. Rakha, I.O. Ellis, D.G. Powe, The oestrogen receptor coactivator CARM1 has an oncogenic effect and is associated with poor prognosis in breast cancer, Breast Cancer Res. Treat. 140 (2013) 307–316, https://doi.org/10.1007/s10549-013-2614-y.
[17] N. Nakayama, G. Sakashita, Y. Nariai, H. Kato, K. Sinmyozu, J. Nakayama, S. Kyo, T. Urano, K. Nakayama, Cancer-related transcription regulator protein NAC1 forms a protein complex with CARM1 for ovarian cancer progression, Oncotarget 9 (2018) 28408–28420, https://doi.org/10.18632/oncotarget.25400.
[18] Y. Wang, W. Zhou, J. Wang, X. Huang, Y. Zuo, T. Wang, X. Gao, Y. Xu, S. Zou, Y. Liu, J. Cheng, Q. Lei, Arginine methylation of MDH1 by CARM1 inhibits glutamine metabolism and suppresses pancreatic cancer, Mol. Cell 64 (2016) 673–687, https://doi.org/10.1016/j.molcel.2016.09.028.
[19] R. Elakoum, G. Gauchotte, A. Oussalah, M. Wissler, C. Clement-Duchene, J. Vignaud, J. Gueant, F. Namour, CARM1 and PRMT1 are dysregulated in lung cancer without hierarchical features, Biochimie 97 (2014) 210–218, https://doi.org/10.1016/j.biochi.2013.10.021.
[20] S.M. Greenblatt, N. Man, P. Hamard, T. Asai, D. Karl, C. Martinez, D. Bilbao, V. Stathias, A.M. Jermakowicz, S. Duffort, M. Tadi, E. Blumenthal, S. Newman, L. Vu, Y. Xu, F. Liu, S.C. Schurer, M.T. McCabe, R.G. Kruger, M. Xu, F. Yang, D. G. Tenen, J. Watts, F. Vega, S.D. Nimer, CARM1 is essential for myeloid leukemogenesis but dispensable for normal hematopoiesis, Cancer Cell 33 (2018) 1111–1127.e5, https://doi.org/10.1016/j.ccell.2018.05.007.
[21] K.J. Veazey, D. Cheng, K. Lin, O.D. Villarreal, G. Gao, M. Perez-Oquendo, H.T. Van, S.A. Stratton, M. Green, H. Xu, Y. Lu, M.T. Bedford, M.A. Santos, CARM1 inhibition reduces histone acetyltransferase activity causing synthetic lethality in CREBBP/EP300-mutated lymphomas, Leukemia 34 (2020) 3269–3285, https://doi.org/10.1038/s41375-020-0908-8.
[22] Q. Feng, B. He, S. Jung, Y. Song, J. Qin, S.Y. Tsai, M. Tsai, B.W. O'Malley, Biochemical control of CARM1 enzymatic activity by phosphorylation, J. Biol. Chem. 284 (2009) 36167–36174, https://doi.org/10.1074/jbc.M109.065524.
[23] K. Higashimoto, P. Kuhn, D. Desai, X. Cheng, W. Xu, Phosphorylation-mediated inactivation of coactivator-associated arginine methyltransferase 1, Proc. Natl. Acad. Sci. U.S.A. 104 (2007) 12318–12323, https://doi.org/10.1073/pnas.0610792104.
[24] C.S. Lim, D.L. Alkon, Protein kinase C stimulates HuD-mediated mRNA stability and protein expression of neurotrophic factors and enhances dendritic maturation of hippocampal neurons in culture, Hippocampus 22 (2012) 2303–2319, https://doi.org/10.1002/hipo.22048.
[25] S. Carascossa, P. Dudek, B. Cenni, P. Briand, D. Picard, CARM1 mediates the ligand-independent and tamoxifen-resistant activation of the estrogen receptor alpha by cAMP, Genes Dev. 24 (2010) 708–719, https://doi.org/10.1101/gad.568410.
[26] N.C. Chang, M. Sincennes, F.P. Chevalier, C.E. Brun, M. Lacaria, J. Segales, P. Munoz-Canoves, H. Ming, M.A. Rudnicki, The dystrophin glycoprotein complex regulates the epigenetic activation of muscle stem cell commitment, Cell, Stem Cell. 22 (2018) 755–768.e6, https://doi.org/10.1016/j.stem.2018.03.022.
[27] S. Suresh, S. Huard, T. Dubois, CARM1/PRMT4: making its mark beyond its function as a transcriptional coactivator, Trends Cell Biol. 31 (2021) 402–417, https://doi.org/10.1016/j.tcb.2020.12.010.

[28] X. Zhong, X. Yuan, Y. Xu, M. Yin, W. Yan, S. Zou, L. Wei, H. Lu, Y. Wang, Q. Lei, CARM1 methylates GAPDH to regulate glucose metabolism and is suppressed in liver cancer, Cell Rep. 24 (2018) 3207–3223, https://doi.org/10.1016/j.celrep.2018.08.066.

[29] F. Liu, F. Ma, Y. Wang, L. Hao, H. Zeng, C. Jia, Y. Wang, P. Liu, I.M. Ong, B. Li, G. Chen, J. Jiang, S. Gong, L. Li, W. Xu, PKM2 methylation by CARM1 activates aerobic glycolysis to promote tumorigenesis, Nat. Cell Biol. 19 (2017) 1358–1370, https://doi.org/10.1038/ncb3630.

[30] T. Abeywardana, M. Oh, L. Jiang, Y. Yang, M. Kong, J. Song, Y. Yang, CARM1 suppresses de novo serine synthesis by promoting PKM2 activity, J. Biol. Chem. 293 (2018) 15290–15303, https://doi.org/10.1074/jbc.RA118.004512.

[31] Y. Cho, Y.K. Kim, ROS-mediated cytoplasmic localization of CARM1 induces mitochondrial fission through DRP1 methylation, Redox Biol. 73 (2024) 103212, https://doi.org/10.1016/j.redox.2024.103212.

[32] Y. Cho, J.W. Hwang, N. Park, J. Moon, K.H. Ali, Y.H. Seo, I.S. Kim, S. Kim, Y. K. Kim, SPC-180002, a SIRT1/3 dual inhibitor, impairs mitochondrial function and redox homeostasis and represents an antitumor activity, Free Radic. Biol. Med. 208 (2023) 73–87, https://doi.org/10.1016/j.freeradbiomed.2023.07.033.

[33] M.B. Davis, X. Liu, S. Wang, J. Reeves, A. Khramtsov, D. Huo, O.I. Olopade, Expression and sub-cellular localization of an epigenetic regulator, co-activator arginine methyltransferase 1 (CARM1), is associated with specific breast cancer subtypes and ethnicity, Mol. Cancer 12 (2013), https://doi.org/10.1186/1476-4598-12-40, 40-40.

[34] A.E. Drew, O. Moradei, S.L. Jacques, N. Rioux, A.P. Boriack-Sjodin, C. Allain, M. P. Scott, L. Jin, A. Raimondi, J.L. Handler, H.M. Ott, R.G. Kruger, M.T. McCabe, C. Sneeringer, T. Riera, G. Shapiro, N.J. Waters, L.H. Mitchell, K.W. Duncan, M. P. Moyer, R.A. Copeland, J. Smith, R. Chesworth, S.A. Ribich, Identification of a CARM1 inhibitor with potent in vitro and in vivo activity in preclinical models of multiple myeloma, Sci. Rep. 7 (2017) 17993–z, https://doi.org/10.1038/s41598-017-18446-z.

[35] B. Perillo, M. Di Donato, A. Pezone, E. Di Zazzo, P. Giovannelli, G. Galasso, G. Castoria, A. Migliaccio, ROS in cancer therapy: the bright side of the moon, Exp. Mol. Med. 52 (2020) 192–203, https://doi.org/10.1038/s12276-020-0384-2.

[36] Y. Son, Y. Cheong, N. Kim, H. Chung, D.G. Kang, H. Pae, Mitogen-activated protein kinases and reactive oxygen species: how can ROS activate MAPK pathways? J. Signal. Transduct. 2011 (2011) 792639 https://doi.org/10.1155/2011/792639.

[37] K. Nakayama, M.M. Szewczyk, C. Dela Sena, H. Wu, A. Dong, H. Zeng, F. Li, R.F. de Freitas, M.S. Eram, M. Schapira, Y. Baba, M. Kunitomo, D.R. Cary, M. Tawada, A. Ohashi, Y. Imaeda, K.S. Saikatendu, C.E. Grimshaw, M. Vedadi, C. H. Arrowsmith, D. Barsyte-Lovejoy, A. Kiba, D. Tomita, P.J. Brown, TP-064, a potent and selective small molecule inhibitor of PRMT4 for multiple myeloma, Oncotarget 9 (2018) 18480–18493, https://doi.org/10.18632/oncotarget.24883.

[38] G. Gao, S. Hausmann, N.M. Flores, A.M. Benitez, J. Shen, X. Yang, M.D. Person, S. Gayatri, D. Cheng, Y. Lu, B. Liu, P.K. Mazur, M.T. Bedford, The NFIB/CARM1 partnership is a driver in preclinical models of small cell lung cancer, Nat. Commun. 14 (2023) 363–y, https://doi.org/10.1038/s41467-023-35864-y.

[39] L. Wang, P. Charoensuksai, N.J. Watson, X. Wang, Z. Zhao, C.G. Coriano, L.R. Kerr, W. Xu, CARM1 automethylation is controlled at the level of alternative splicing, Nucleic Acids Res. 41 (2013) 6870–6880, https://doi.org/10.1093/nar/gkt415.

[40] D. Shlensky, J.A. Mirrielees, Z. Zhao, L. Wang, A. Mahajan, M. Yu, N.M. Sherer, L. G. Wilke, W. Xu, Differential CARM1 isoform expression in subcellular compartments and among malignant and benign breast tumors, PLoS One 10 (2015) e0128143, https://doi.org/10.1371/journal.pone.0128143.

[41] L. Wang, Z. Zhao, M.B. Meyer, S. Saha, M. Yu, A. Guo, K.B. Wisinski, W. Huang, W. Cai, J.W. Pike, M. Yuan, P. Ahlquist, W. Xu, CARM1 methylates chromatin remodeling factor BAF155 to enhance tumor progression and metastasis, Cancer Cell 30 (2016) 179–180, https://doi.org/10.1016/j.ccell.2016.06.013.